

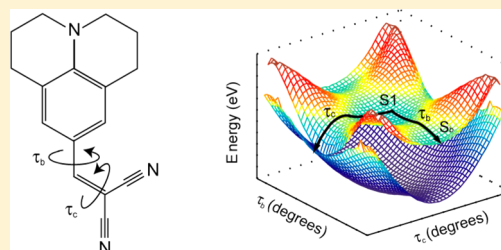
Resolving Photo-Induced Twisted Intramolecular Charge Transfer with Vibrational Anisotropy and TDDFT

Wenkai Zhang,[†] Zhenggang Lan,[‡] Zheng Sun,[†] and Kelly J. Gaffney^{*,†}[†]PULSE Institute, SLAC National Accelerator Laboratory, Stanford University, Menlo Park, California, 94025, United States[‡]Qingdao Institute of Bioenergy and Bioprocess Technology, Chinese Academy of Sciences, Qingdao, 266101, Shandong, China

S Supporting Information

ABSTRACT: The interplay between reaction environment and photochemical outcome has wide ranging implications for designing and directing light driven chemical conversions. We present a detailed mechanistic description of photoisomerization in julolidine malononitrile (JDMN) as the first step to characterizing this interplay between reaction pathways and reaction environment. We have used polarization resolved UV pump–mid-IR probe spectroscopy and time dependent DFT calculations to investigate the dynamics of charge transfer induced intramolecular rotation in JDMN. We have probed the mechanism and dynamics of photoisomerization with the symmetric and antisymmetric CN-stretch of the malononitrile group.

These measurements show the S1 electronic excited state relaxes with a 12.3 ps time constant by isomerizing around both the C–C single and C–C double bond of the malononitrile group with a branching ratio of 1:5. Isomerization around the single bond leads to the formation of a metastable twisted excited state, while isomerization around the double bond leads to excited state quenching via a conical intersection between the S1 and S0 electronic states. We have characterized the electronic and nuclear structure of the long-lived excited state with pump–probe anisotropy measurements and time dependent DFT calculations using the CAM-B3LYP functional and the 6-31G(d,p) basis set. These calculations further confirm that isomerization around the malononitrile single bond forms a twisted intermolecular charge transfer excited state.



■ INTRODUCTION

A robust understanding of the interplay between reaction environment and photochemical outcome has wide ranging implications for designing and directing light driven chemical conversions, as well as the developing of molecular sensors of local physical properties. Both short-range Pauli exclusion driven steric effects and long-range electrostatic effects should be important, making modifications in the viscoelastic and dielectric properties of the reaction environment likely important. Previous studies have emphasized the solvent viscosity dependence of photoisomerization dynamics, such as the extensive studies of stilbene photoisomerization dynamics.¹ Other studies have emphasized the role of excited state charge transfer, like the twisted intramolecular charge transfer proposed to explain the dual fluorescence of 4-(*N,N*-dimethylamino)-benzonitrile (DMABN).² Progressing beyond our current understanding requires a description of the dual importance of viscoelastic and electrostatic effects, a goal that will be enhanced by dynamical studies that more directly and comprehensively assess the photoisomerization dynamics.

Here, we utilize polarization resolved UV pump–mid-IR probe measurements to robustly characterize the isomerization dynamics of julolidinemalononitrile (JDMN) dissolved in dimethylsulfoxide (DMSO). Figure 1 shows the molecular structure of JDMN, which is also known as 9-(2,2-dicyanovinyl)julolidine (DCVJ). Three critical attributes determine the success of this experiment. (1) The CN-stretch

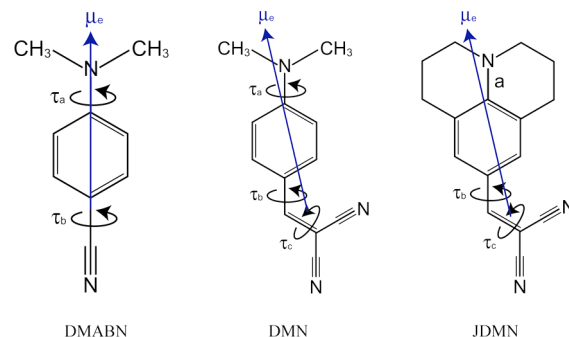


Figure 1. Molecular structures of *para*-dimethylaminobenzonitrile (DMABN), *para*-dimethylalaninemalononitrile (DMN), and *para*-julolidinemalononitrile (JDMN). The figure also shows the S0 → S1 electronic transition dipole and the torsional angles potentially involved in the S1 electronic excited state relaxation dynamics.

vibrations of the malononitrile functional group form two local modes, a symmetric and antisymmetric stretch, decoupled from the rest of the molecule. This proves critical to theoretical modeling of the signal, since the direction of the vibrational transition dipole moment can differ significantly between

Received: June 29, 2012

Revised: August 22, 2012

Published: August 30, 2012

ground and excited states for normal modes involving the motion of many atoms in the molecule. The comparative ease of interpreting the orientational dependence of local mode vibrations also distinguishes UV pump – mid-IR probe measurements from a transient electronic or Raman probe.^{3–12} (2) As schematically shown in Figure 2, the bond

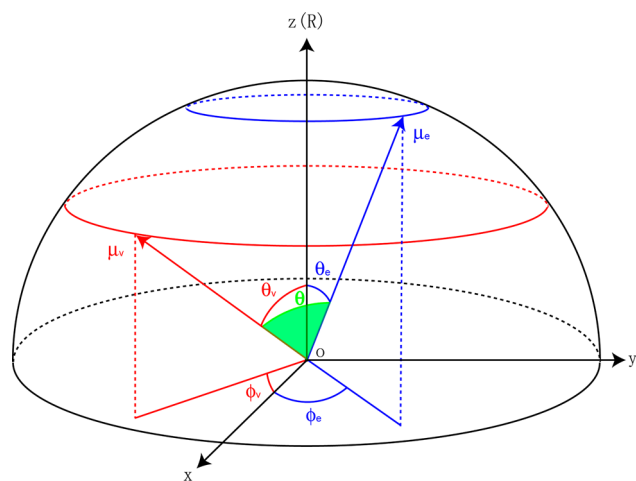


Figure 2. Schematic view of how the photoinduced change in the torsional angle, $\Delta\phi$, can be extracted from the polarization resolved UV pump–mid-IR probe measurement. The definitions of the labels in the figure can be found in the Experimental Methodology section.

isomerization must change the projection of the probed vibrational transition dipole moment onto the electronic transition dipole moment for the signal to be sensitive to the change in molecular structure. (3) The change in structure in the laboratory frame needs to be similar to the change in structure in the molecular frame. This can be achieved when the isomerizing bond separates the molecule into two components with very different moments of inertia, a requirement met by JDMN, but not by stilbene or azobenzene.

JDMN, like DMABN and 2-[4-(dimethylamino)-benzylidene]malononitrile (DMN), represent characteristic members of a general class of disubstituted benzenes with donor (D) and acceptor (A) substituents in the para positions. The chromophores of GFP and photoactive yellow protein also reside in this general class of push–pull D-phenyl-A complexes. For DMN, the electronically excited molecule can isomerize around bonds labeled a, b, and c in Figure 1, with variations in the reaction environment potentially influencing the branching ratio. In JDMN, the orientational constraints introduced by linking the alkyl chain to the benzene ring inhibit isomerization about bond a.

Several investigations of photoinduced processes in benzyliidenemalononitriles have preceded our studies and demonstrated the sensitivity of the photochemical dynamics to the details of the reaction environment.^{13–29} The strong correlation between the fluorescence quantum yield and the solvent viscosity highlights the potential importance of viscoelastic effects, but the absorption and emission spectra also show strong solvatochromism highlighting the potential importance of solvent electrostatic effects.^{13,14} While numerous studies have attempted to use the photoinduced dynamics of DMN and JDMN to probe the polarity and microviscosity of solvents,^{14–19} polymers,^{20–23} ionic liquids,^{24–26} and biological media^{27–29} without a mechanistic understanding of the

environmental properties that govern the excited state dynamics, benzyliidenemalononitriles have limited value as molecular sensors.

The multiple excited state isomerization pathways that can be followed in DMN and JDMN also present a potentially important means of studying the interplay between photochemical dynamics and reaction environment, but to date no experiment has proven capable of determining the isomerization branching ratios for either molecule. While previous studies assign the fast nonradiative quenching of the S1 excited state to efficient S1 → S0 internal conversion, disagreement remains regarding which photoisomerization pathway dominates.^{13–15,18,19,21–24,26–30} Some authors have suggested photoisomerization occurs around bond b,^{22,24,26–29} bond c,^{18,19,21,23} or various combinations of a, b, and c.^{13–15,18,21} Quantum chemical studies have also been utilized to investigate which photoisomerization pathway dominates,^{13,15,30} but the excited state potential energy surfaces prove to be sensitive to the theoretical method utilized, highlighting the importance of experimental characterization.

Through the use of polarization resolved UV pump–mid-IR probe spectroscopy and time dependent DFT calculations, we have determined the branching ratio for isomerization around bonds b and c in JDMN and the rate of these bond isomerizations, we have identified a long-lived twisted intramolecular charge transfer excited state generated by isomerization about bond b, and we have characterized the orientational relaxation dynamics on the S1 electronic excited state potential energy surface.

■ EXPERIMENTAL METHODOLOGY

We used DMSO and JDMN purchased from Sigma Aldrich without further purification. We used a 200 μm thick rotating sample cell with two CaF_2 windows for pump–probe measurements on a 20 mM JDMN solution in DMSO. Rotating the sample cell reduces the rate of slow UV-induced sample damage. We prepared all samples with an optical density around 1 at both 400 nm and 2210 cm^{-1} . The pump and probe pulses were generated with a Ti:sapphire regenerative amplifier laser system (Spitfire, Spectra-Physics) with a 1 kHz repetition rate, 2.5 mJ pulse energy, 800 nm central wavelength, and a 50 fs full width at half-maximum (fwhm) pulse duration. The 400 nm pump pulse was produced by frequency-doubling one portion of the amplifier output with a 0.1 mm thick BBO crystal. We generated tunable mid-IR probe pulses by difference frequency mixing the output of a near-IR optical parametric amplifier (OPA800CF, Spectra-Physics) in AgGaS_2 . These mid-IR pulses have a duration of roughly 70 fs fwhm with spectral width of about 200 cm^{-1} fwhm. We crossed the pump and probe beams in a rotational sample cell, with a probe diameter of 100 μm and a pump diameter of 400 μm . We used 2–5 μJ of 400 nm radiation for each pump pulse. We dispersed the transmitted probe beam with a grating spectrometer (iHR320, Horiba JobinYvon) onto a liquid nitrogen cooled 32×2 MCT pixel array detector (FPAS-6416-D, Infrared Systems Development Corp.) with a spectral resolution of 4 cm^{-1} per pixel.

Polarization resolved UV pump–mid-IR probe spectroscopy measures the isotropic, $I_{\text{iso}}(t) = I_{\parallel}(t) + 2I_{\perp}(t)$, and the anisotropic, $r(t) = (I_{\parallel}(t) - I_{\perp}(t))/I_{\text{iso}}(t)$, signals from the parallel polarization (I_{\parallel}) and perpendicular polarization (I_{\perp}) signals. The anisotropy can be related to the relative angle between the electronic and vibrational transition dipole

moments, θ . When the molecular axes remain fixed in the laboratory frame during the time period between the pump and probe pulses, $r = (2/5)\langle P_2(\cos \theta) \rangle$, where $P_2(x) = (3x^2 - 1)/2$.^{31–34} Note that we measure the ensemble average of the second-order Legendre polynomial, not the ensemble average of θ . As shown in Figure 2, photoinduced bond isomerization can lead to a change in the angle θ and the measured anisotropy. We place the rotational axis R along the z axis, since the rotational axis is invariant in the molecular frame. The electronic transition dipole moment μ_e is defined by the tilt angle θ_e between R and μ_e and the in-plane rotation angle ϕ_e . Similarly, the vibrational transition dipole moment μ_v is defined by the tilt angle θ_v between R and μ_v and the in-plane rotation angle ϕ_v . The relative angles θ between μ_e and μ_v can be easily correlated to the molecular structure through the following relationship: $\cos \theta = \cos \theta_e \cos \theta_v - \sin \theta_e \sin \theta_v \cos \phi$, where $\phi = \phi_e - \phi_v$ is the dihedral angle between the $R\mu_e$ and the $R\mu_v$ planes. We measure the angle θ and calculate the two tilt angles, θ_e and θ_v , allowing us to determine the bond rotation angle, ϕ , from our combined experimental and computational study.

Figure 2 also highlights the critical requirements for an anisotropic pump–probe measurement to be sensitive to bond isomerization. First, neither the pump transition dipole moment, μ_e , nor the probe transition dipole moment, μ_v , can lie parallel to R . Second, the directions of the vibrational transition dipole moment must be accurately determined for electronic excited states and cannot be assumed to be equivalent to the directions in the electronic ground state. Thus, the proposed rotation of the phenyl-amine bond of DMABN, labeled bond a in Figure 1, cannot be identified by time-resolved anisotropy measurements because μ_e and R are parallel.

EXPERIMENTAL RESULTS

Figure 3 shows the $S_0 \rightarrow S_1$ electronic absorption spectrum and the CN-stretch vibrational absorption of JDMN. The single vibrational absorption, despite the presence of two nitrile groups, reflects the similar transition energies of the symmetric and antisymmetric CN-stretches and the much larger absorption cross-section for the symmetric stretch, as will be addressed in the theoretical results section. We excited the $S_0 \rightarrow S_1$ transition of JDMN at 400 nm¹⁴ and measured the transient absorption dynamics using the nitrile stretch vibrations between 2090 and 2230 cm^{−1} with the mid-IR probe pulse polarization parallel and perpendicular to the pump pulse polarization.^{10,31,33,35,36} We generate the isotropic, $I_{\text{iso}}(t) = I_{\parallel}(t) + 2I_{\perp}(t)$, and the anisotropic, $r(t) = (I_{\parallel}(t) - I_{\perp}(t))/I_{\text{iso}}(t)$, signals from the parallel polarization (I_{\parallel}) and perpendicular polarization (I_{\perp}) signals.

The I_{\parallel} and I_{\perp} spectra for a 1, 20, and 100 ps time delay are shown in Figure 4, and the full isotropic transient absorption spectra appear in the Supporting Information. The increased transmission centered at 2210 cm^{−1} corresponds to the ground state bleach (GSB) signal and provides a clear monitor of the electronic ground state recovery dynamics. Figure 4A shows two clearly distinct reductions in mid-IR transmission centered at 2112 and 2160 cm^{−1} corresponding to excited-state absorption (ESA) bands. The signal measured with a time delay of 20 ps, shown in Figure 4B, has an additional band with a negative change in transmitted intensity at 2200 cm^{−1}. By a time delay of 100 ps, the transient signal at 2200 cm^{−1} has

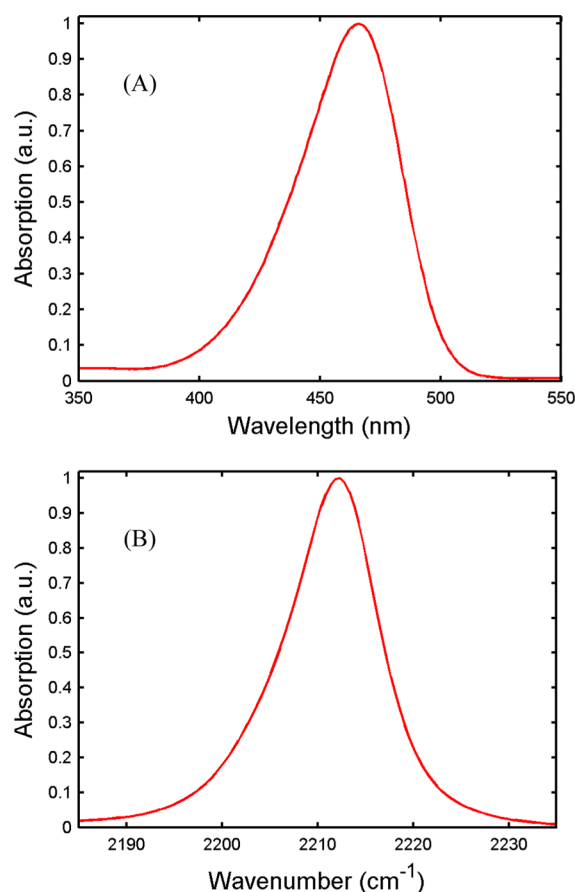


Figure 3. (A) UV–visible and the (B) mid-IR absorption spectra of JDMN in DMSO.

decayed to zero and the ESA absorptions centered at 2112 and 2160 cm^{−1} have shifted to 2106 and 2155 cm^{−1} (Figure 4C).

Figure 5A shows the time-dependent isotropic signal for JDMN in DMSO measured at three different central frequencies: 2210 (GSB), 2155 (ESA), and 2115 cm^{−1} (ESA). As will be discussed in detail in the theoretical calculations section, we assign the ESA at 2155 cm^{−1} to the symmetric CN-stretch and the ESA at 2115 cm^{−1} to the antisymmetric CN-stretch. The GSB provides a clear measure of the electronic ground state recovery dynamics. The electronic ground state has a biphasic recovery, with the majority of the relaxation occurring with a 25 ± 5 ps time constant, and the remaining recovery occurring with a 152 ± 50 ps time constant. These biexponential recovery dynamics clearly indicate that the excited state decay occurs via two distinct pathways.

These distinct pathways also influence the dynamics measured with the ESA, but in a more complex manner. The symmetric and antisymmetric CN-stretching vibrations of the S_1 excited state and the long-lived excited state that relaxes with a 152 ps time constant cannot be distinguished spectrally. This causes the decay of the S_1 ESA signal to overlap with the rise and decay of the long-lived excited state. The additional excited state absorption centered at 2200 cm^{−1} also appears and decays at intermediate delay times. The fast relaxation of the GSB and ESA bands at 2115 and 2155 cm^{−1} correlates with the rise time for the ESA band at 2200 cm^{−1}, but the decay of this band occurs with a much faster 25 ps time constant than the decay time for the long-lived ESA at 2115 and 2155 cm^{−1}. We

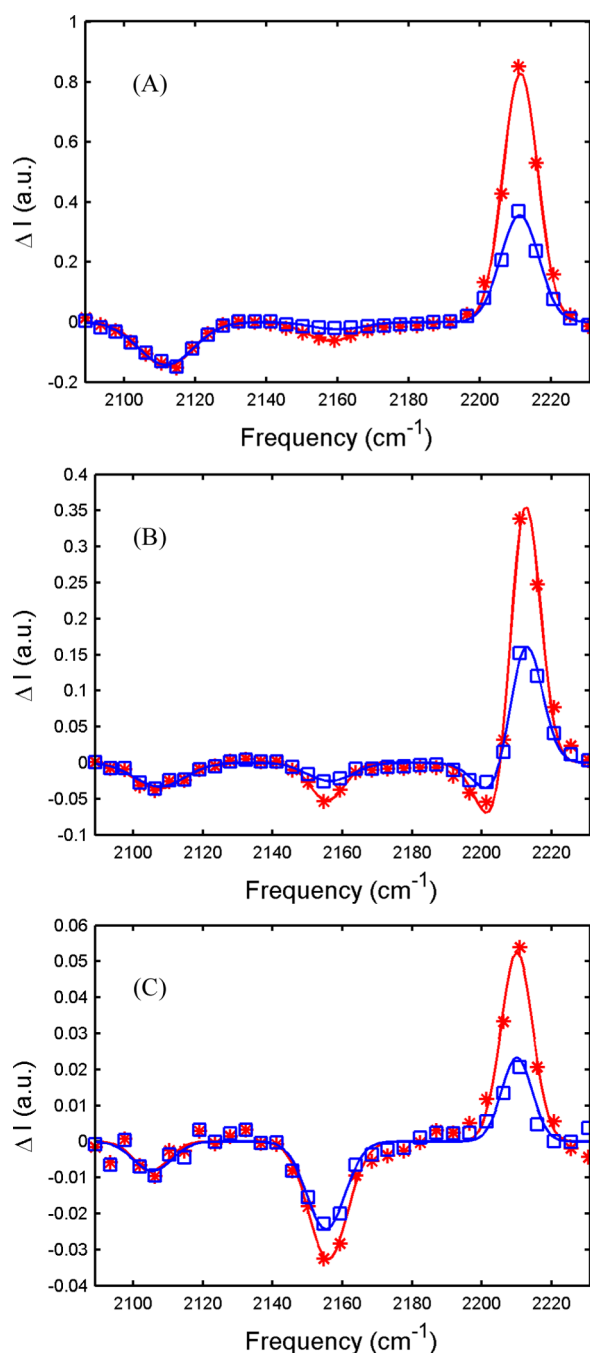


Figure 4. Pump–probe parallel polarization (red asterisk) and pump–probe perpendicular polarization (blue square) transient spectra for JDMN in DMSO at (A) 1, (B) 20, and (C) 100 ps time delays. The solid line shows the fit of the transient spectra to the model discussed in the Experimental Results section and presented in detail in the Supporting Information.

attribute this excited state absorption to the vibrationally excited S_0 state of JDMN, S_0^* , where anharmonic coupling between the CN-stretching bands and vibrationally excited low frequency bands leads to a hot band shift that decays with the rate of vibrational relaxation.

We conclude from the kinetic data discussed above that the photoinduced dynamics of JDMN in DMSO follows two S_1 excited state decay channels. The assignment of these decay channels will be addressed in the Discussion. We have modeled the S_1 electronic excited state decay kinetics with two parallel

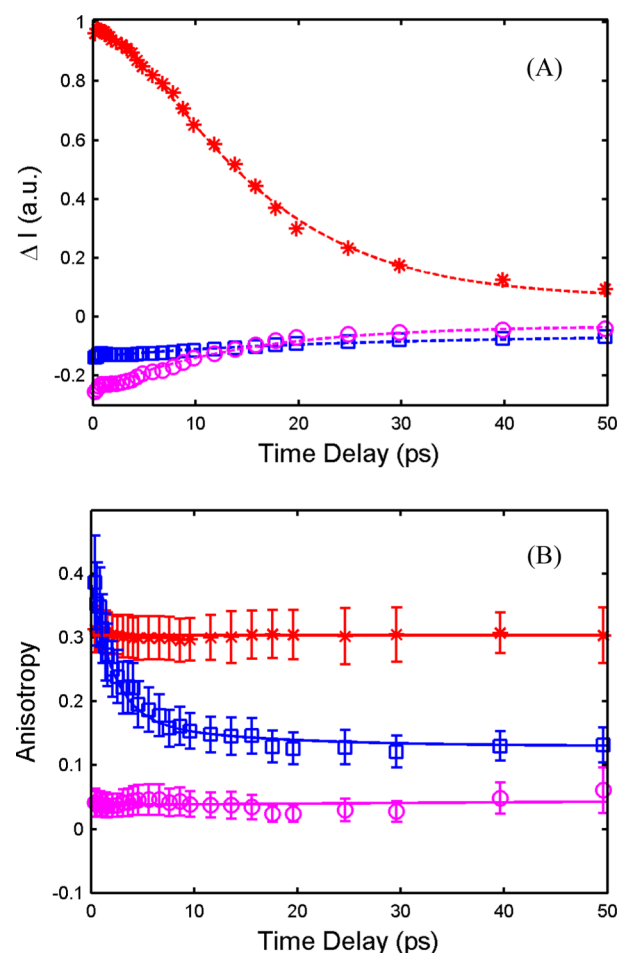


Figure 5. (A) Time-dependent change in transmission for the isotropic pump–probe signal. Population dynamics for the GSB measured at 2210 cm^{-1} (red asterisk), the ESA band measured at 2155 cm^{-1} (blue square), and the ESA band measured at 2115 cm^{-1} (purple circle) of JDMN measured in DMSO. (B) Time-dependent anisotropy for JDMN in DMSO at three different spectra range: 2210 cm^{-1} (red asterisk), 2155 cm^{-1} (blue square), and 2115 cm^{-1} (purple circle). Error bars are included for each data point. The solid lines show the kinetic model fit to the experimental data.

relaxation channels each involving two sequential relaxation steps:



where S_1 corresponds to the electronic excited state populated by UV excitation, S_0^* corresponds to the vibrationally excited electronic ground state, S_b corresponds to the long-lived excited state, and S_0 represents the electronic ground state. The following rate constants govern the chemical kinetics: k_{11} corresponds to the rate of decay from S_1 to S_0^* , k_{12} the rate of vibrational relaxation from S_0^* to S_0 , k_{21} the rate of decay from S_1 to S_b , and k_{22} the rate of S_b relaxation to S_0 . The details of the population dynamics that result from this kinetic model can be found in the Supporting Information. The fit of the full two-dimensional isotropic data using these kinetic equations, along with Gaussian lineshapes for the peaks in the vibrational spectrum, appears in the Supporting Information. A fit of the single frequency kinetics with this kinetic model can also be

found in Figure 5A. Table 1 summarizes the rate constants and excited-state CN-stretch frequencies that generate the best fit to the experimental data.

Table 1. CN-Stretch Vibrational Frequencies and Kinetic Time Constants Extracted from the Global Fit of the Experimental Data

	experimental fit	anisotropy	angle $\langle\theta\rangle$
$\omega_{S1}^{(as)}$	$2109 \pm 6 \text{ cm}^{-1}$	0.04 ± 0.03	51 ± 3
$\omega_{S1}^{(ss)}$	$2165 \pm 3 \text{ cm}^{-1}$	0.39 ± 0.05	8 ± 8
$\omega_{Sb}^{(as)}$	$2104 \pm 8 \text{ cm}^{-1}$	0.04 ± 0.03	51 ± 3
$\omega_{Sb}^{(ss)}$	$2155 \pm 9 \text{ cm}^{-1}$	0.13 ± 0.03	42 ± 3
ω_{S0^*}	$2209 \pm 5 \text{ cm}^{-1}$	NA	NA
ω_{S0}	$2211 \pm 1 \text{ cm}^{-1}$	0.31 ± 0.04	23 ± 5
$(k_{11} + k_{21})^{-1}$	$12.3 \pm 0.8 \text{ ps}$	NA	NA
k_{12}^{-1}	$25 \pm 5 \text{ ps}$	NA	NA
k_{22}^{-1}	$152 \pm 50 \text{ ps}$	NA	NA

While the isotropic signal provides clear access to the chemical kinetics, this data provides limited structural information about the isomerization mechanism or the nature of the distinct relaxation pathways followed by JDMN. We measured the time-resolved vibrational anisotropy to address these structural questions. Figure 5(B) shows the time-dependent anisotropy measured at three different central frequencies: 2210 (GSB), 2155 (ESA), and 2115 cm^{-1} (ESA). The GSB has an initial anisotropy of 0.31 ± 0.04 which does not show any decay in the first 50 ps following UV excitation. This clearly demonstrates that JDMN rotation occurs on a time scale much slower than 50 ps. The slow rate of molecular rotation confirms that the time dependent changes in the ESA anisotropies result from excited state bond isomerization and the increased rotational flexibility of JDMN in the S1 excited electronic state. This allows the anisotropy values of the symmetric and antisymmetric CN-stretch bands at long time delays, when the S1 excited state signal will have fully decayed, to be used to assess the structure of the long-lived excited state. This assignment will be addressed in the Discussion.

The ESA anisotropy measured at 2115 cm^{-1} shows an initial value of 0.04 ± 0.03 which also shows no measurable time dependence within the statistical accuracy of the measurement, indicating the S1 and S_b electronic excited states have very similar antisymmetric CN-stretch anisotropies. The ESA anisotropy measured at 2155 cm^{-1} has pronounced time dependence, starting from an initial value of 0.39 ± 0.05 that decays to 0.13 ± 0.03 within the 50 ps time window shown in Figure 5B. The spectral indistinguishability of the CN symmetric stretch in the S1 and S_b excited states complicates the analysis of the anisotropy data. The Supporting Information provides a detailed description of how the population dynamics extracted from the isotropic signal enables a robust analysis of the time-resolved anisotropy. Here we highlight the key results of this analysis. The measured anisotropy corresponds to a weighted sum of the S1, $r_{S1}^{(ss)}$, and S_b, $r_{Sb}^{(ss)}$, anisotropies

$$r_{\text{ESA}}^{(ss)}(t) = \frac{I_{S1}(t)}{I_{S1}(t) + I_{Sb}(t)} r_{S1}^{(ss)}(t) + \frac{I_{Sb}(t)}{I_{S1}(t) + I_{Sb}(t)} r_{Sb}^{(ss)}(t) \quad (2)$$

where the isotropic signals can be used to fully account for the time dependent signal strengths, I_{S1} and I_{Sb} . The nature of the

population dynamics discussed previously also allows us to determine the value of the anisotropy for the symmetric CN-stretch of the S1 and the S_b excited states. The initial value of the anisotropy, $r_{S1}^{(ss)}(t = 0 \text{ ps}) = 0.39$, provides the starting value for the S1 excited state since the long-lived excited state has yet to form, while the anisotropy measured for time delays long compared to the S1 relaxation time, $r_{Sb}^{(ss)}(t = 50 \text{ ps}) = 0.13 \pm 0.03$, provides the value for the S_b excited state. Given the different values of the anisotropy for the two distinct excited states, the time dependent change in S1 and S_b excited state populations would lead to a time dependent anisotropy, even if $r_{S1}^{(ss)}$ and $r_{Sb}^{(ss)}$ were time independent. This time dependence would match the 12.3 ps time constant associated with the decay of the S1 state and the rise of the S_b state, but the anisotropy decay occurs much faster than this time constant would allow. This strongly indicates that $r_{S1}^{(ss)}$ has a time dependent decay. We have fit $r_{S1}^{(ss)}$ to a single exponential with an offset, $r_{S1}^{(ss)} = A \exp(-t/\tau) + C$. The best fit to the experimental data shown in Figure 5B gives $\tau = 2.6 \pm 0.7 \text{ ps}$, $A = 0.21 \pm 0.04$, and $C = 0.18 \pm 0.03$. The Supporting Information demonstrates in detail the inability of the population dynamics to account for the measured anisotropy dynamics.

The value of the anisotropy provides the angle between the electronic transition dipole moment, μ_e , and the vibrational transition dipole moment, μ_v , when molecular rotation can be ignored. The theoretical framework for describing the relation between the measured anisotropy and the molecular structure has been discussed in the Experimental Methodology section. The anisotropy for the S_b electronic excited state, coupled with the quantum chemical calculations, provides the critical information for determining the structure of the long-lived excited state. The anisotropy values measured for the GSB and the ESA at nominally zero time delay provide critical information for validating the quantum chemical methodology used to characterize the structure of the S_b electronic excited state. The value of the angle θ between μ_e and μ_v determined from the experimental anisotropy appears in Table 1. The comparison with the predictions of the theoretical molecular structures and values for μ_e and μ_v will be addressed in the Discussion.

CALCULATION RESULTS

Our study focuses on the generation of a structural and dynamical model self-consistent with both experiment and quantum chemical calculations. This has been achieved by balancing computational speed and accuracy. Our choice of an appropriate electronic-structure method and basis set focused on two key considerations. First, the electronic excited states of JDMN possess charge-transfer character that must be treated accurately. We have chosen to use the CAM-B3LYP functional which has been demonstrated to successfully treat the long-range Coulomb interactions critical for the description of valence excited states and charge-transfer states.³⁷ The success of prior benchmark studies^{37–40} support the use of TDDFT with CAM-B3LYP functional to treat the electronic excited states of JDMN. The computational expense of evaluating the Hessian matrix necessary for calculating the vibrational frequencies provides the second key constraint for identifying a feasible but accurate quantum chemical methodology.

We tested a variety of functional and basis sets before focusing our efforts on the CAM-B3LYP functional and the 6-

31G(d,p) basis set. A comparison of the $S_0 \rightarrow S_1$ vertical excitation energy obtained with different functionals and basis sets can be found in the Supporting Information. The $S_0 \rightarrow S_1$ transition involves a shift of electron density from the julolidine group toward the malononitrile group. This charge redistribution leads to a change in the molecular dipole from 11.0 D for S_0 to 14.9 D for S_1 . The calculated electron transition dipole moment, μ_e , for the $S_0 \rightarrow S_1$ excitation lies nearly parallel to the principle inertial axis of JDMN, as shown in the Supporting Information.¹³

The vertical excitation energies calculated with TDDFT using the CAM-B3LYP functional and the 6-31G(d,p) basis set exceed the experimental values by roughly 0.4 eV. While this error in the vertical excitation energy exceeds that of other functionals, we have chosen to utilize CAM-B3LYP because of its quality performance in benchmark studies of charge-transfer excited states.^{37–40} Larger basis sets show a modest improvement in the agreement between the calculated and measured vertical excitation energy, but given the time-consuming nature of the vibrational analysis, our calculations have emphasized the 6-31G(d,p) basis set. The inclusion of solvent effects by using a polarized continuum solvent model reduces the calculated excitation energy, but does not modify the main features of the potential energy surfaces, as shown in the Supporting Information.

We have calculated the minimum-energy geometries for the S_0 and S_1 electronic states. The TDDFT/CAM-B3LYP calculations predict the presence of one structural minimum on the S_1 potential energy surface (PES) near the Franck–Condon region. The calculated PES energy varies weakly with torsion of bond b and bond c, consistent with significant torsional flexibility and dynamics in the S_1 excited state. The minimum potential energy of the S_0 and S_1 electronic states as a function of torsional angles τ_b and τ_c appear in Figure 7. When bond c twists to $\tau_c \approx 80\text{--}90^\circ$ the DFT calculation breaks down due to formation of biradical structures in the ground-state electronic wave function. Nonetheless, the calculations are consistent with the presence of a conical intersection between S_1 and S_0 near $\tau_c \approx 90^\circ$.^{13,15,30} This provides a reasonable explanation for the ultrafast decay of the S_1 electronic excited state population back to a vibrationally excited electronic ground state S_0^* . The S_0 and S_1 two-dimensional rigid scan PES calculated along the torsional angles τ_b and τ_c appear in the Supporting Information. As will be addressed in the Discussion, the shallow S_1 torsional PES can be utilized to explain the orientational dynamics observed for the S_1 excited state.

These quantum chemical calculations can be utilized to assess the properties of the excited state species observed experimentally. We first address the ground electronic state structure. Figure 6A shows the S_0 minimum-energy geometry. The whole molecule has a planar structure, including the julolidine and the malononitrile groups. The calculated values for the symmetric and antisymmetric CN-stretch vibrational frequencies, vibrational intensity, transition dipole directions, and the angle θ between μ_e and μ_v in S_0 appear in Table 2.

We then searched the electronic excited state PES for energetic minima associated with metastable twisted structures. We identified two different minima using TDDFT calculations with the CAM-B3LYP functional and 6-31G(d,p) basis set, though only one involves significant molecular rotation. The structures associated with these minima appear in Figure 6. As we mentioned above, one minimum occurs in the Franck–Condon region with a structure very similar to the S_0 minimum

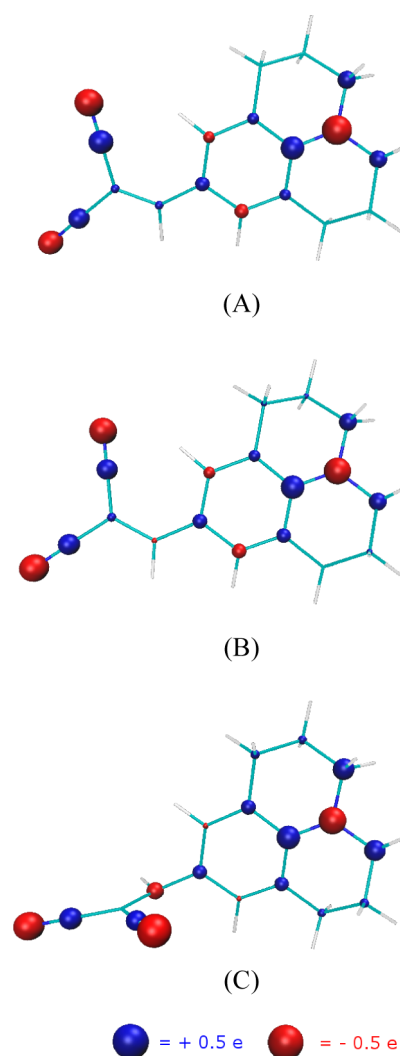


Figure 6. Mulliken atomic charge distribution with hydrogens summed into heavy atoms for the S_0 , S_1 , and S_b electronic states in their minimum energy nuclear configurations. Blue spheres denote positive charges and red spheres negative charges.

energy configuration. The depth of this minimum is too shallow to trap the excited state population and cannot account for the long-lived excited state structure. The second PES minimum occurs at $\tau_b = 80^\circ$ and corresponds to a distinct electronic excited state which we labeled as S_b . Since $\tau_b \approx 0^\circ$ for both the S_0 and the S_1 minimum energy structures, this gives a rotational angle $\Delta\phi = 80^\circ$ for bond b rotation. The calculated values for the symmetric and antisymmetric CN-stretch vibrational frequencies, vibrational intensity, transition dipole directions, and the angle θ between μ_e and μ_v in S_1 and S_b also appear in Table 2. These θ and the anisotropy values that can be calculated from them prove to be central to our determination of the S_b long-lived excited state molecular structure which will be addressed in the Discussion.

Two differences in the electronic structure of S_1 and S_b clearly identify S_b as a twisted intramolecular charge transfer state. The S_b electronic dipole moment exceeds that of S_1 by 6.2 D. First, the 6.2 D increase in dipole moment between S_1 and S_b originates from the transfer of charge from the julolidine π electron system to the malononitrile π electron system. Second, the isomerization of bond b decouples the π electron systems of the julolidine and malononitrile groups. These two

Table 2. Calculated Properties of the Symmetric and Anti-Symmetric CN-Stretching Vibrations for the S₀, S₁, and S_b Electronic States

assignment		ω (cm ⁻¹)		IR intensity (km/mol)	dipole derivative			θ
		exp	calc		x	y	z	
S ₀	as	NA	2200.3	24.1	−0.41	4.87	0.39	95.0
	ss	2211 ± 1	2210.3	153.9	12.40	−0.47	−0.09	2.0
S ₁	as	2109 ± 6	2121.7	79.5	3.56	8.14	−0.76	66.6
	ss	2165 ± 3	2163.0	4.6	2.11	−0.35	−0.06	9.3
S _b	as	2104 ± 8	2095.0	345.7	13.50	−4.58	11.94	50.1
	ss	2155 ± 9	2165.8	94.4	9.22	−0.41	−3.05	33.7

properties in combination demonstrate that the transition from S₁ to S_b involves electron transfer between molecular orbitals that have been decoupled by isomerization around bond b, the defining feature of TICT.² These changes in charge distribution and structure can be found in Figure 6.

DISCUSSION

The experimental results can be roughly split into isotropic pump–probe data that can be used to construct a kinetic model and anisotropic pump–probe data that can be used to determine the structural properties of the photoinduced electronic excited states populated in the kinetic model. We used the TDDFT/CAM-B3LYP excited state potential energy surfaces to construct a model and arrived at a self-consistent understanding of the photoisomerization and the excited state relaxation dynamics in JDMN.

The dynamics measured with the isotropic transient absorption demonstrate that the S₁ electronic excited state populated by UV excitation decays with a time constant of 12.3 ± 0.8 ps. The biexponential ground state recovery and the presence of the long-lived excited state absorption clearly show that the S₁ excited state has two decay channels. We use the relative amplitudes of the two exponential components in the ground state recovery to get the branching ratio for the two decay channels which results from the relative relaxation rates for formation of S_b and S₀*, $\Phi = [(k_{21}(k_{11} + k_{21} - k_{12})]/[k_{11}(k_{11} + k_{21} - k_{22})] = 0.11$. This gives a time constant of $k_{11}^{-1} = 14.8 \pm 0.9$ ps for relaxation from S₁ to S₀* and a time constant of $k_{21}^{-1} = 73 \pm 8$ ps for relaxation from S₁ to S_b. These intermediate excited states, S₀* and S_b, correspond to the vibrational excited electronic ground state and the bond b isomerized electronic excited state, respectively. S₀* relaxation results from vibrational energy transfer from JDMN to the DMSO solvent and occurs with a time constant of $k_{12}^{-1} = 25 \pm 5$ ps. S_b relaxes back to the S₀ electronic ground state with a time constant of $k_{22}^{-1} = 152 \pm 50$ ps.

We attribute the two relaxation pathways to isomerization around either bond b or bond c. For both channels to contribute measurable S₀* and S_b intermediate populations requires the S₁ PES to either have barriers of similar height for torsion around bonds b and c or effectively no barriers. The TDDFT calculation generates a barrier of 59 meV between the S₁ potential energy minimum at $\tau_b, \tau_c \approx 0^\circ$ and the conical intersection with S₀ generated when isomerizing around τ_c and a slightly larger barrier of 72 meV between the S₁ potential energy minimum at $\tau_b, \tau_c \approx 0^\circ$ and the metastable intermediate S_b formed when isomerizing around τ_b . The lower barrier for isomerization around bond c would predict k_{11} to be larger than k_{12} , consistent with measurement, but the difference generated by a variation in barrier height, when assuming full equilibration on the S₁ potential, would generate a factor of 2 difference in

the rates rather than the factor of 5 measured. The level of agreement between experiment and calculation may be fortuitous given the intrinsic errors in the calculations, the sensitivity of the S₁ potential to the methodological details,¹³ the absence of equilibration on the S₁ excited state PES, and the neglect of solvent effects.

The S₁ excited state lifetime can be compared to the fluorescence lifetime of JDMN in DMSO measured by Maroncelli and co-workers.¹⁴ While they observe a similar time constant of 5.3 ps, the difference in the time constants clearly exceeds the measurement accuracies of both studies. The origin of the different rates remains unclear, but one potential explanation would be non-Condon effects in the fluorescence cross-section. As will be discussed below we have strong experimental and computation evidence in support of large orientational excursions on the S₁ electronic excited state prior to bond isomerization. If the fluorescence cross-section dropped as the excited molecules sampled the torsional phase space of the S₁ PES, it could account for the faster rate of fluorescence decay. The study of Maroncelli and co-workers did not observe evidence for two relaxation pathways. This indicates the S_b electronic excited state has much lower fluorescence yield than the S₁ electronic excited state, consistent with the charge transfer character of the S_b electronic excited state. The calculation of the oscillator strength for the S₁ → S₀ transition significantly exceeds the oscillator strength for the S_b → S₀ transition which can be found in the Supporting Information. The dominance of S₁ excited state relaxation to the S₀ electronic ground state via isomerization around bond c agrees with the previous quantum chemical calculations performed by Maroncelli and co-workers on the related dimethylaniline malononitrile molecule.¹³

The time-resolved anisotropy data shown in Figure 5B complements the isotropic dynamics and when combined with the calculated excited state structures allows us to determine the structures associated with the distinct electronic excited states. Before discussing the excited state anisotropies we will address the anisotropy of the GSB signal. The small frequency difference between the two CN-stretches, 2200 and 2210 cm⁻¹, agrees with the appearance of a single CN-stretch absorption peak for the electronic ground state molecule at 2210 cm⁻¹ in the experiment. As discussed in the Supporting Online Information, we can use the calculated electronic transition dipole direction, the vibrational absorption cross sections, and the vibrational transition dipole directions for the symmetric and the antisymmetric CN-stretches to predict the value of the anisotropy for the GSB signal. This gives a calculated GSB anisotropy of $r_{\text{GSB}} = 0.32$, nearly equivalent to the experimental value of 0.31 ± 0.04 . This agreement between measured and calculated anisotropy helps validate the theoretical analysis of

not only the vibrational frequencies, but also the absorption cross sections and transition dipole moment directions.

The S1 PES minimum has a structure very similar to the S0 PES minimum, making $\Delta\phi \approx 0^\circ$. The TDDFT calculation gives symmetric and antisymmetric CN-stretch frequencies of 2163.0 and 2121.7 cm^{-1} , respectively, for the molecular structure associated with the energy minimum on the S1 PES. The calculated values strongly resemble the experimental values for the S1 electronic excited state of 2165 and 2109 cm^{-1} and allow us to assign the 2165 cm^{-1} peak to the symmetric CN-stretch and the 2109 cm^{-1} peak to the antisymmetric CN-stretch. While the minimum energy molecular structure on the S1 PES differs slightly from the minimum energy structure on the S0 PES, the electronic excitation changes the vibrational transition dipole moment directions. The angle between the symmetric CN-stretch vibrational transition dipole moment and electronic transitional dipole moment is $\theta_{S1}^{(ss)} = 9.3^\circ$, while the angle is $\theta_{S1}^{(as)} = 66.6^\circ$ for the antisymmetric stretch. The experimental value of $\theta_{S1}^{(ss)} = 8 \pm 8^\circ$ measured at a time delay of 0.5 ps strongly resemble the angle predicted by the TDDFT calculations, but the experimental value of $\theta_{S1}^{(as)} = 51 \pm 3^\circ$ differs significantly from the calculated value. The origin of this discrepancy remains unclear.

The S_b electronic excited state generated by torsion about bond b has calculated symmetric and antisymmetric CN stretch frequencies of 2165.8 and 2095.0 cm^{-1} , respectively. These values agree with the ESA vibrational frequencies measured at long time delays, 2155 and 2104 cm^{-1} , within 10 cm^{-1} and allow for robust peak assignments. The angle between the symmetric CN-stretch vibrational transition dipole moment and electronic transition dipole moment is $\theta_{S1}^{(ss)} = 33.7^\circ$, while the angle is $\theta_{S1}^{(as)} = 50.1^\circ$ for the antisymmetric stretch. The experimental values of $\theta_{S1}^{(ss)} = 42 \pm 3^\circ$ and $\theta_{S1}^{(as)} = 51 \pm 3^\circ$ measured at time delay long compared to the relaxation of the S1 electronic excited state resemble the angles predicted by the TDDFT calculations. This agreement allows us to robustly assign the long-lived excited state to the calculated molecular structure associated with the calculated S_b electronic excited state.

This analysis presumes that the bond rotation in the molecular frame matches the bond rotation in the laboratory frame. Bond isomerization in a dense media like a solvent may also involve the rotation of the whole molecule to minimize the need for solvent reorganization. In time-resolved anisotropy studies of *cis*-stilbene by Sension et al.,⁵ they concluded that photoisomerization roughly conserved the size and shape of the solvent cavity occupied by *cis*-stilbene. This requires rotation of the full molecule, as well as rotation about the isomerizing bond. While this represents a potentially significant complication to the data analysis, the issue should be much more pronounced for *cis*-stilbene than JDMN. For *cis*-stilbene both phenyl ring have equivalent volumes, so minimizing the change in the solvent cavity requires significant molecular rotation in the laboratory frame. For JDMN, the julolidine group has a much larger volume than the malononitrile group, so minimizing the change in the solvent cavity associated with torsion about bond b will emphasize motion of the malononitrile group and comparatively little rotation of the full molecule. This supports our use of a molecular frame analysis.

The fast orientational relaxation of the S1 excited state symmetric CN-stretch will be the last topic of discussion. As mentioned briefly in the Experimental Results section and

discussed in detail in the Supporting Information, we have used a biexponential model to fit the S1 excited state symmetric CN-stretch orientational relaxation data. We will now use the restricted orientational diffusion model of Lipari and Szabo to interpret this biexponential fit.^{41,42} While the original model presumes the probe transition dipole is parallel to the pump transition dipole at time zero, Ji and Gaffney have shown that it can be included in models that also allow nonparallel pump and probe transition dipole moments.⁴³ Since the initial value of the anisotropy, $r_{S1}^{(ss)} = 0.39 \pm 0.05$, nearly equals 0.4, we ignore the deviation from parallel pump and probe transition dipole moments.

Within this model, fast orientational diffusion with diffusion constant, D_ϕ , can occur within a restricted cone of semiangle θ_ϕ , after which the cone orientationally diffuses on the surface of the full sphere with a second diffusion constant, D_θ . While the exact expression for $C_2(t)$ in the restricted orientational diffusion model involves an infinite sum of exponentials,^{41,42} an accurate approximation can be made for cone semiangles $\theta_c < 60^\circ$. The approximate model gives

$$C_2(t) = S^2 \exp(-6D_\theta t) + [1 - S^2] \exp(-t[1/\tau_{\text{eff}} + 6D_\theta]) \quad (3)$$

Within this model, $1 - S^2$ represents the fraction of the anisotropy that decays due to orientational diffusion within the restricted cone, τ_{eff} represents the characteristic time for orientational diffusion within the cone, and D_θ represents the orientational diffusion constant for diffusion outside of the cone. The cone semiangle can be determined from $S^2 = \langle P_2(\cos \theta_c) \rangle^2$, where $P_2(x) = (3x^2 - 1)/2$. The slow component of the orientational relaxation equals 0.18 ± 0.03 of $r(t)$, or 0.45 ± 0.08 of $C_2(t)$, and $\theta_c = 28 \pm 3^\circ$. The magnitude of the cone semiangle qualitatively conforms with the shape of the S1 PES along the τ_b and τ_c torsional angles shown in Figure 7.

The restricted orientational diffusion model also allows the orientational diffusion constant for orientational relaxation within the cone, D_c , to be determined from D_θ and τ_{eff} . First, the experimental analysis gives $\tau_{\text{eff}} = 2.6 \pm 0.7$ ps, since D_θ effectively equals zero. Lipari and Szabo provide an approximate solution for D_c from τ_{eff} and θ_c when $\theta_c < 60^\circ$

$$D_c \tau_{\text{eff}} (1 - S^2) = -x_0^2 (1 + x_0)^2 \{ \ln[(1 + x_0)/2] + (1 - x_0)/2 \} / [2(1 - x_0)] + (1 - x_0)(6 + 8x_0 - x_0^2 - 12x_0^3 - 7x_0^4)/24 \quad (4)$$

where $x_0 = \cos \theta_c$. Using the values listed above we get $D_c^{-1} = 70 \pm 20$ ps. While wobbling in a cone orientational diffusion provides a rather approximate description of the non-equilibrium orientational dynamics of photoexcited JDMN, the parametrization of the range of orientational freedom and rate of motion reflected by θ_c and D_c may provide additional benchmarks for assessing quantum dynamics calculations and the influence of the reaction environment on JDMN photochemical dynamics.

■ CLOSING REMARKS

Understanding how the physical properties of an engineered reaction environment dictates the outcome of photoisomerization reactions has wide ranging implications for designing and

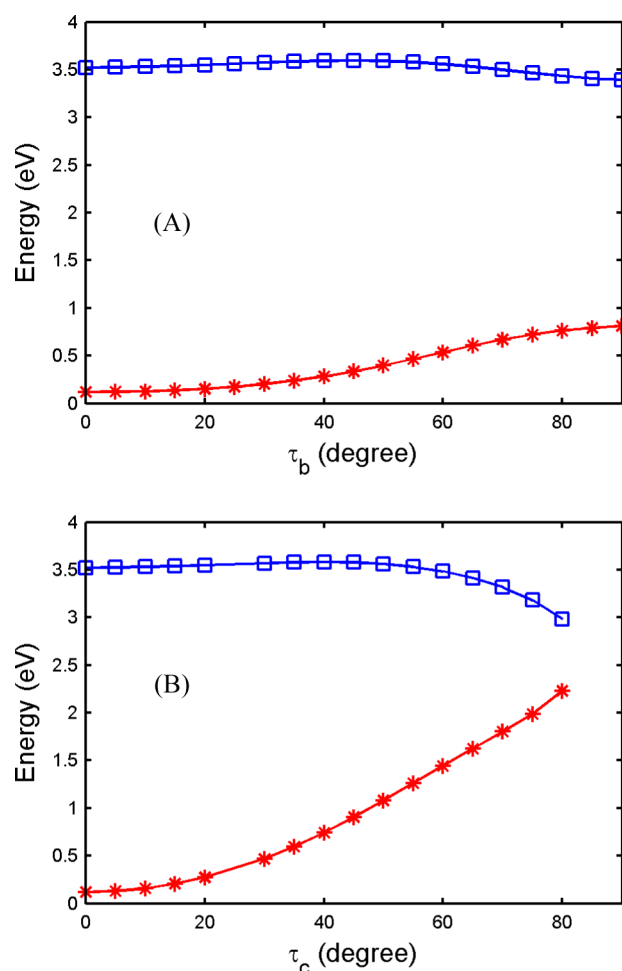


Figure 7. (A) One-dimensional relaxed PES for the S0 and S1 electronic states as a function of τ_b . The potential has a barrier of height 72 meV at $\tau_b \approx 45^\circ$. (B) One-dimensional relaxed PES for the S0 and S1 electronic states as a function of τ_c . The potential has a barrier of height 59 meV at $\tau_c \approx 40^\circ$.

directing light driven chemical conversions, as well as the development of molecular sensors of local physical properties.

A multitude of scientists using a variety of methods are pursuing this question, but detailed and robust characterization of electronic excited state chemical dynamics often proves difficult. Here we demonstrate that polarization resolved UV pump–mid-IR probe measurements in conjunction with time dependent DFT calculations can be used to measure photoisomerization branching ratios and rates, determine the nuclear and electronic structure of long-lived excited states, and characterize the orientational flexibility of molecules in electronic excited states. All these properties provide an excellent means of characterizing the influence of the reaction environment on photochemical dynamics with a greater level of detail than time-resolved fluorescence or pump–probe measurements in the visible and UV. The combination of these measurements and TDDFT calculations has confirmed photoisomerization generates a metastable twisted intramolecular charge transfer excited state. The combination of bond rotation and electron redistribution highlights the dual importance of electrostatic and viscoelastic effects in photoisomerization and sets the stage for future studies directed at determining how variations in the reaction environment influence photochemical pathways.

■ ASSOCIATED CONTENT

Supporting Information

Kinetic modeling of the experimental population dynamics; error propagation for the anisotropy measurements; extracting anisotropic signals associated with distinct molecular excited states with overlapping vibrational bands; calculation; from the molecular frame to the laboratory frame; theoretically calculated geometries for S0, S1, and S_b. This material is available free of charge via the Internet at <http://pubs.acs.org>.

■ AUTHOR INFORMATION

Corresponding Author

*E-mail: kgaffney@slac.stanford.edu.

Notes

The authors declare no competing financial interest.

■ ACKNOWLEDGMENTS

W.Z. and K.G. thank Dr. Ji, Robert Hartsock, and Winnie Liang and Z.L. thanks Professor A. Sobolewski for helpful discussions. W.Z., Z.S., and K.G. acknowledge support from the AMOS program within the Chemical Sciences, Geosciences, and Biosciences Division of the Office of Basic Energy Sciences, Office of Science, U.S. Department of Energy. Z.L. thanks the partial support from the CAS 100 Talent Project, from NSFC (No. 21103213), and from the Director Innovation Foundation of CAS-QIBEBT.

■ REFERENCES

- (1) Waldeck, D. H. *Chem. Rev.* **1991**, *91*, 415–436.
- (2) Grabowski, Z. R.; Rotkiewicz, K.; Rettig, W. *Chem. Rev.* **2003**, *103*, 3899–4031.
- (3) Wallin, S.; Davidsson, J.; Modin, J.; Hammarstrom, L. *J. Phys. Chem. A* **2005**, *109*, 4697–4704.
- (4) Iwata, K.; Weaver, W. L.; Gustafson, T. L. *Chem. Phys. Lett.* **1993**, *210*, 50–54.
- (5) Sension, R. J.; Repinec, S. T.; Szarka, A. Z.; Hochstrasser, R. M. *J. Chem. Phys.* **1993**, *98*, 6291–6315.
- (6) Todd, D. C.; Jean, J. M.; Rosenthal, S. J.; Ruggiero, A. J.; Yang, D.; Fleming, G. R. *J. Chem. Phys.* **1990**, *93*, 8658–8668.
- (7) Baskin, J. S.; Banares, L.; Pedersen, S.; Zewail, A. H. *J. Phys. Chem.* **1996**, *100*, 11920–11933.
- (8) Chang, C. W.; Lu, Y. C.; Wang, T. T.; Diau, E. W. G. *J. Am. Chem. Soc.* **2004**, *126*, 10109–10118.
- (9) Haran, G.; Morlino, E. A.; Matthes, J.; Callender, R. H.; Hochstrasser, R. M. *J. Phys. Chem. A* **1999**, *103*, 2202–2207.
- (10) Heyne, K.; Mohammed, O. F.; Usman, A.; Dreyer, J.; Nibbering, E. T. J.; Cusanovich, M. A. *J. Am. Chem. Soc.* **2005**, *127*, 18100–18106.
- (11) Douhal, A.; Sanz, M.; Tormo, L. *Proc. Natl. Acad. Sci. U.S.A.* **2005**, *102*, 18807–18812.
- (12) Poprawa-Smoluch, M.; Baggerman, J.; Zhang, H.; Maas, H. P. A.; De Cola, L.; Brouwer, A. M. *J. Phys. Chem. A* **2006**, *110*, 11926–11937.
- (13) Swalina, C.; Maroncelli, M. *J. Phys. Chem. C* **2010**, *114*, 5602–5610.
- (14) Jin, H.; Liang, M.; Arzhantsev, S.; Li, X.; Maroncelli, M. *J. Phys. Chem. B* **2010**, *114*, 7565–7578.
- (15) Allen, B. D.; Benniston, A. C.; Harriman, A.; Rostron, S. A.; Yu, C. F. *Phys. Chem. Chem. Phys.* **2005**, *7*, 3035–3040.
- (16) Loutfy, R. O.; Arnold, B. A. *J. Phys. Chem.* **1982**, *86*, 4205–4211.
- (17) Loutfy, R. O.; Law, K. Y. *J. Phys. Chem.* **1980**, *84*, 2803–2808.
- (18) Mqadmi, S.; Pollet, A. *J. Photochem. Photobiol. A-Chem.* **1990**, *53*, 275–281.
- (19) Safarzadehamiri, A. *Chem. Phys. Lett.* **1986**, *129*, 225–230.
- (20) Loutfy, R. O. *Pure Appl. Chem.* **1986**, *58*, 1239–1248.

- (21) Hooker, J. C.; Torkelson, J. M. *Macromolecules* **1995**, *28*, 7683–7692.
- (22) Dreger, Z. A.; White, J. O.; Drickamer, H. G. *Chem. Phys. Lett.* **1998**, *290*, 399–404.
- (23) Jee, A. Y.; Bae, E.; Lee, M. J. *Phys. Chem. B* **2009**, *113*, 16508–16512.
- (24) Gutkowsky, K. I.; Japas, M. L.; Aramendia, P. F. *Chem. Phys. Lett.* **2006**, *426*, 329–333.
- (25) Jin, H.; Li, X.; Maroncelli, M. J. *Phys. Chem. B* **2007**, *111*, 13473–13478.
- (26) Paul, A.; Samanta, A. J. *Phys. Chem. B* **2008**, *112*, 16626–16632.
- (27) Kung, C. E.; Reed, J. K. *Biochemistry* **1989**, *28*, 6678–6686.
- (28) Iwaki, T.; Torigoe, C.; Noji, M.; Nakanishi, M. *Biochemistry* **1993**, *32*, 7589–7592.
- (29) Haidekker, M. A.; Theodorakis, E. A. *Org. Biomol. Chem.* **2007**, *5*, 1669–1678.
- (30) Lan, Z. G.; Lu, Y.; Weingart, O.; Thiel, W. J. *Phys. Chem. A* **2012**, *116*, 1510–1518.
- (31) Lim, M. H.; Jackson, T. A.; Anfinrud, P. A. *Nat. Struct. Biol.* **1997**, *4*, 209–214.
- (32) Hansen, P. A.; Moore, J. N.; Hochstrasser, R. M. *Chem. Phys.* **1989**, *131*, 49–62.
- (33) Moore, J. N.; Hansen, P. A.; Hochstrasser, R. M. *Proc. Natl. Acad. Sci. U.S.A.* **1988**, *85*, 5062–5066.
- (34) Lim, M.; Jackson, T. A.; Anfinrud, P. A. *Science* **1995**, *269*, 962–966.
- (35) Usman, A.; Mohammed, O. F.; Nibbering, E. T. J.; Dong, J.; Solntsev, K. M.; Tolbert, L. M. *J. Am. Chem. Soc.* **2005**, *127*, 11214–11215.
- (36) Ansari, A.; Szabo, A. *Biophys. J.* **1993**, *64*, 838–851.
- (37) Dreuw, A.; Head-Gordon, M. *Chem. Rev.* **2005**, *105*, 4009–4037.
- (38) Rudberg, E.; Salek, P.; Helgaker, T.; Agren, H. J. *Chem. Phys.* **2005**, *123* (184108), 1–7.
- (39) Jacquemin, D.; Wathelet, V.; Perpète, E. A.; Adamo, C. J. *Chem. Theory Comput.* **2009**, *5*, 2420–2435.
- (40) Plotner, J.; Tozer, D. J.; Dreuw, A. J. *Chem. Theory Comput.* **2010**, *6*, 2315–2324.
- (41) Lipari, G.; Szabo, A. *Biophys. J.* **1980**, *30*, 489–506.
- (42) Lipari, G.; Szabo, A. *J. Am. Chem. Soc.* **1982**, *104*, 4546–4559.
- (43) Ji, M. B.; Gaffney, K. J. *J. Chem. Phys.* **2011**, *134* (044516), 1–13.